High-Resolution Gamma-Ray Imaging Measurements using Externally Segmented Germanium Detectors

J. L. Callas, W. A. Mahoney, R. T. Skelton, L. S. Varnell and Wm. A. Wheaton
Jet Propulsion Laboratory, Pasadena, California 91109

ABSTRACT

Fully two-dimensional gamma-ray imaging with simultaneous high-resolution spectroscopy has been demonstrated using an externally segmented germanium sensor. The system employs a single high-purity coaxial detector with its outer electrode segmented into 5 distinct charge collection regions and a lead coded aperture with a uniformly redundant array (URA) pattern. A series of one-dimensional responses was collected around 511 keV while the system was rotated in steps through 180°. A non-negative, linear least-squares algorithm was then employed to reconstruct a 2-dimensional image. Corrections for multiple scattering in the detector, and the finite distance of source and detector arc made in the reconstruction process.

INTRODUCTION

Gamma-ray lines provide direct information on a number of fundamental astrophysical problems including nucleosynthesis, high-energy processes near compact objects, and solar flare physics. An understanding of these processes will require observations with instrumentation that combines high sensitivity, excellent energy resolution, and high angular resolution. Our approach to achieve these capabilities involves the use of JPL-developed position-sensitive (externally segmented) germanium detectors [1,2] in combination with appropriate coded apertures.

Unlike radiation at lower energies, gamma rays cannot be reflected or refracted in practical imaging systems. Therefore, other imaging techniques must be employed. Coded apertures in conjunction with position sensitive detectors have been used successfully for hard x-rays and gamma rays [3,4] to construct imaging systems extending the simple pin hole camera concept.[5] However, high spatial resolution 2-dimensional position sensitive germanium detectors have proved difficult to fabricate in the large volumes needed above 100 keV. We have combined a large volume germanium detector externally segmented to achieve fine (~0.5 cm) spatial resolution in one dimension, with a 1-dimensional coded aperture. By rotating the system and combining many 1-dimensional exposures from various orientations, a fully 2-dimensional image can be reconstructed with techniques analogous to tomography (i.e., CAT-scans).[6]

APPARATUS

A prototype gamma-ray imaging system capable of simultaneous imaging and high-resolution spectroscopy has been developed at JPL. The system includes a position-sensitive detector, a coded aperture, a means of simulating system rotation and a data acquisition system. A diagram of the laboratory set up is shown in Figure 1.

To construct a position-sensitive germanium detector, the outer electrode of a coaxial germanium detector is segmented into distinct charge collecting regions.[1] The segmentation technique was developed at Lawrence Berkeley Laboratory (LBL) and is described by Luke.[7] A detector 5.3 cm long has been divided by this process into five segments, each approximately 1.06 cm long. Its performance has been described in Varnell et al.[8] When a gamma ray interacts in the detector, a pulse is produced at the center electrode that is proportional to the energy deposited in the entire detector. In addition, pulses are produced at the external electrode of each segment in which an interaction occurred during the absorption of the gamma ray. Techniques for constructing the detector capsule, front-end electronics, and cryostat with feedthroughs have been developed in a

joint program between JPI. and LBL. A second 5-segment detector has been produced by LBL and tested at JPL. A 12--scgmcnt, large-vo]umc detector has recently been completed and is currently undergoing tests at JPL.

The coded aperture was fabricated at JPL using lead bricks machined into aperture elements 20 cm x 5 cm x 1.06 cm. The 1.06 cm dimension was chosen to match the average segment thickness of the germanium detector. The elements of the aperture were arranged to form two cycle.s of order 5 minus one clement of a Uniformly Redundant Array (URA).[9] The pattern is shown below with shaded squares representing CLOSLXI elements.

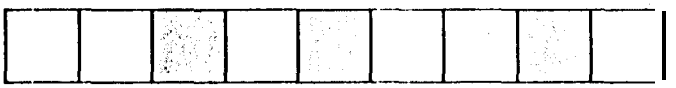

This particular choice of pattern has been shown by Monte Carlo study to be very successful in producing images (using an exact algebraic deconvolutional technique) without artifacts while permitting high transmission.[9*10,11]

The aperture was positioned such that its elements were parallel to the detector segments, as *shown* in Figure 1. The separation from the detector axis to the front face of the coded aperture was 40 cm. This results in an intrinsic one-dimensional angular resolution (d/I,) of 1.06 cm/40 cm -1.5°. The resulting one-dimensional pixels or stripes have a width of 1.5°. Only haIf of each outside stripe is fully coded limiting the total instrument FOV to 6°. Of course, other separations arc possible resulting in different angular resolutions and instrument FOVs.

To achieve fully two-dimensional operation, the one-dimensional system of detector and coded aperture must be rotated relative to the gamma-ray sour-cc. To simplify the laboratory apparatus and operation, the gamma-ray source field instead of the imaging system was rotated through 180°. A protractor with 180° rotation and 30 cm radial adjustment was used to rotate the gamma-ray source field in discrete steps through 180°.

A Macintosh-based data acquisition system was developed using commercial CAMAC and NJM electronic modules. The system digitized the pulse heights from each of the five external segments and from the central electrode of the germanium detector using two EG&G Ortec AD413 units. A central electrode signal between adjustable lower-level and upper-]cvcl discriminators was used to trigger an event. For each event, the digitized signal from each segment and central electrode was stored on disk for off-line analysis.

OPERATION

The gamma-ray source was positioned 4.0 m from the axial center-line of the germanium detector. The source distance was constrained by available laboratory space. The coded aperture position was then chosen as a compromise between the need to minimize the effect due to the finite source distance and to maximize angular resolution for (he system,

In order to collect the information necessary to reconstruct a single 2-dimensional image, 13 separate gamma-ray exposures were collected. Table 1 summarizes the separate exposures indicating source and aperture conditions. The collection time for all exposures was 5.0×10^4 seconds. The dead-time was virtually negligible (-0.2%) in all cases. A calibrated ^{22}Na point source (511 kcV) of activity 2.33x1 0^5 becquerel (Bq) was used.

'1'able 1

Exposure Data Set	Coded Aperture present	Source present	Source Field Rotation
	no	no	n/a
2	no	ycs	n/a
3	yes	no	n/a
4	yes	yes	0°
5	yes	yes	18°
6	yes	ycs	36°
7	yes	yes	54°
8	yes	yes	72°
9	yes	ycs	900
10	yes	yes	108°
11	yes	yes	126°
12	ycs	yes	144°
13	yes	yes	162°

Exposure 1 established the room background levels which were subtracted from the Exposure 2 measurements to yield the net response, or effective area, in each segment. Exposure 3 established the room background level with the coded aperture in place for subtraction from each of the subsequent exposures. Exposures 4 through 13 were the ten exposures collected at successive rotational steps through 180°.

ANALYSIS

With externally segmented germanium detectors, energy depositions can occur in multiple segments from a single incident gamma ray primarily due to Compton scattering. This

complicates the position-location capability of the segmented detector. Techniques developed previously can be applied in the deconvolution process to the multiple-segment event data to resolve which segment was entered by the incoming gamma ray.[10] For analysis, the data were partitioned into sets containing events with only sil~glc-segment interactions and sets with only multiple-segment interactions.

This experiment contained an additional effect duc to beam divergence introduced by the finite distance of the source from the detector. Source strength and laboratory space constrained the source distance to 4.0 m. Detailed Monte Carlo simulations were performed using the ACCEPT[12] code to understand this effect. "l"his effect can be corrected in the deconvolution process with the appropriate treatment in the forward response matrix. Figure 2 illustrates this effect in l-dimension with Monte Carlo events. Of course, this correction is not required when sources arc very distant, e.g., the stars.

Two approaches to the analysis were employed. The first involved using the gamma-ray spectral fitting program, HYPERMET[13] to tally the number of full-energy-peak (FEP) counts associated with each gamma-ray line in the spectrum for each segment (fitted-line technique). Here, the FEP counts, peak centroids and line widths were determined for each exposure set. The second, more complex, technique involved retaining the data in 1 keV energy channels and performing the subsequent analysis for each energy channel (spectral technique). "l'his technique preserves the spectral information of the data in the image deconvolution process. The technique was simplified some by retaining only 200 energy channels between 400 keV and 600 kcV.

Exposures 1 and 2 were analyzed to determine the detector performance. Net FEP counts (fitted-linc technique) and net counts pcr channel (spectral technique) were obtained by subtracting the background data from the source-present data. Dividing the net counts pcr segment by the known source fluence at the source distance resulted in the net segment effective area. The effective area response for each segment at an energy of 511 keV is shown in Figure 3 for both single and rnulti-segment data. Note the larger response from Segment 1 in the single-sc.gmcnt data and the expected lower efficiency for the end segments for the multi-segment data[10]. Segment 1 corresponds to the closed end of the detector and is thicker than the other segments.

The remaining 11 exposures listed in I'able 1 represent the onc background and 10 rotational exposures of the full system. Again, each exposure time was 5.OX104 seconds to simplify the analysis. The net FEP counts (fitted-line technique) and the net counts pcr energy channel (spectral technique) in each segment were tallied for all ten exposure rotations. Figure 4 shows

the background subtracted result from the exposure at 0° rotation for 51 1 keV (fi[tcd-line technique). Note the expected modulation of the coded aperture.

The net FEP counts and net counts per channel for each segment at each rotational position were then divided by the effective area response of the segment to yield the fluence (or differential fluence) $S_{n,k}$, experienced by each segment at each rotation, i.e.,

$$S_{n,k} = (N_{n,k} - I?_{,})/A_n \quad (1)$$

where $N_{n,k}$ is the FEP count tally or counts per channel at rotational position k, B_n is the background count and A_n is the energy dependent effective area response for segment n. (Note that k = 1, 2, ... 10 corresponds to rotations of 0°, 18°, ... 1620.) Equation (1) corrects for detection efficiency of each segment. This process is performed for both the single- and multi-segment data sets using both techniques.

The fluence (or differential fluence) experienced by each segment at each rotation can be expressed as a vector, S with 50 elements (5 segments x 10 rotations) representing the data space. This vector is represented as a 50 element column matrix by stacking each of the ten individual $S_{n,k}$,

$$\mathbf{S} = \begin{vmatrix} S_{1,1} \\ S_{2,1} \\ \cdot \\ \cdot \\ \cdot \\ \cdot \\ S_{5,1\text{C}} \end{vmatrix} \quad (2)$$

Representing the image as an array of source pixels (given a source field of pixels), wc can write the expectation value for each element of the data space S as a linear sum of source pixels

$$\langle s \rangle = \mathbf{D}\phi \quad (3)$$

where ϕ is the vector of fluence from each source. pixel (i. e., the source field) and D is the forward response matrix.

The interpretation of the forward response matrix, D, is straightforward. For a given source field, each element of the response matrix is the fraction of fluence experienced by a given detector segment at a given rotational position from each pixel in the source field as viewed through the coded aperture. This results in a dimensionless matrix. As mentioned previously, multiple scattering in the detector complicates this formulation. However, these effects can be treated with modifications to the forward response matrix.

A Monte Carlo simulation was used to compute the forward response matrix. The Monte Carlo employed the ACCEPT[12] code to simulate the 1 -dimensional response of the instrument set-up including details of the segmented detector, cryostat, coded aperture and the effects of multiple scattering and finite source position. Cases were run for the five source positions (five 1-D stripes) which map out the instrument FOV response. The elements of the l-dimensional response matrix are calculated by tallying the simulated FEP counts from each segment with the coded aperture in place for a given source position. These counts are then divided by the simulated FEP counts for each segment tallied from a simulation with the coded aperture absent. This results in a 5x5 dimensionless (5 segments x 5 stripes) forward response matrix. The 2-dimensional forward response matrix, D is formed by combining the 1-dimensional response matrix from the Monte Carlo simulation with the algebraic calculation of the projection of a 2-dimensional source field onto a 1-dimensional source field for the ten rotational positions used in this experiment. A simple geometric algorithm was developed to calculate the projections. 'l'his two step process for the generation of the forward response matrix, D allows flexibility in the choice of 2-dimensional source field since the instrument specific response is completely contained in the 1-dimensional response formulation.

A deconvolved 2-dimensional image can be determined by solving equation (3) with a linear least-squares algorithm to obtain estimates of $\langle\phi\rangle$ for the source pixels. Since D is not generally square for an over-dctcr]nincd set of equations, a solution can found by inversion of the "normal matrix", $\mathbf{D^TD}$. This solution at a given energy estimates ϕ as

$$\langle\phi\rangle = \left[(\mathbf{D^TD})^{-1}\mathbf{D^T}\right]S \qquad (4)$$

where $\langle\phi\rangle$ is the vector of source pixel estimates for a given energy channel and $\mathbf{D^T}$ is the transpose of the forward response matrix, $\mathbf{D}$. Unfortunately this naive least-squares approach may encounter difficulty in practice duc to strong anticorrelation among adjacent pixels that may overwhelm the expected signal in the resulting images. This is principally duc to spacing the pixel grid of the source field c1osc to or finer than the intrinsic instrument resolution (-d/I.)

which leads to nearly singular normal matrices, with very large elements in the inverse normal matrix, and oscillatory behavior.

Applying the physical requirement that all real sources (pixels) be non-negative has a crucial effect, stabilizing the deconvolution method against ill-conditioning [14]. Positivity forces the negative excursions in the image to rise to zero, and hence it forces the adjacent positive excursion to decrease correspondingly, because of the anti-correlation. The result is to flatten the images, strongly suppressing spurious artifacts. The FORTRAN subroutine NNLS[15], given a forward response matrix **D** and vector S, directly solves the over-determined system represented by Equation (3) for the source pixels ϕ in least-squares sense, subject to the constraint that

$$\phi_j \geq 0. \qquad (5)$$

If NNLS is used, the estimation of the magnitude of the probable errors cannot be done in the standard way. One approach[16], which we take here, is to suppose that zero or negative pixels can simply be omitted from the model, equation (3). Then standard least-squares, on the positive pixels only, will return the same solution as NNLS, since both return the best least-squares solution on the restricted pixel set. Then the variance of the estimate, for the positive pixels only, is

$$\mathrm{Var}[\langle\phi_j\rangle] = \sum_i [(D'll))\text{-}l1)1']ji20i2 \qquad (6)$$

where $\sigma_i^2 = \mathrm{Var}[S_i]$, of the data, and the data index i = (1, ... 50) runs over segments n and rotations k in equation (2). This estimate is not exact, since other random data samples could give different positive pixels, and so different uncertainties. A more rigorous (but more laborious) approach (but only if the true model was known) would be to Monte Carlo a large data sample and tally the pixel estimates that result from NNLS.

With NNLS it has been possible to use much finer pixel grids than without the positivity constraint. For data of very high statistical quality, all pixels in the image may be positive without constraint. On re-analyzing the data with a finer pixel grid, the oscillations appear, and the positivity constraint stabilizes the result. Thus for high-statistics data, the effect of positively is to allow the effective resolution to be pressed beyond what would otherwise be possible. Here the 2-dimensional image resolution of this experiment can be advanced from the intrinsic instrument resolution of 1.5° per pixel to 0.75° per pixel without serious loss of sensitivity.

'1'0 investigate this, two choices of source field were made in this experiment. One choice was a 5x5 field of 1.5 °×1.5° square pixels, with an effective FOV 01' 6°×6°(only half of each outside pixel is fully modulated by the coded aperture in this case). Here the pixel sized match the intrinsic resolution of the 1 -dimensional instrument. This problem was highly over determined, with only 25 pixels (unknowns) and 50 data elements (equations). The other choice was a 7×7 pixel field of 0.75°X0.750 square pixels, with a FOV of 5.25°X5.250. This arrangement has a smaller FOV than the previous choice but fully includes the position of the gamma-ray source. This problem is only slightly over constrained (49 unknowns and 50 equations) and is a factor of two finer in image resolution than the intrinsic resolution of the instrument. Figures 5a and 5b illustrate, respectively, the 5x5 and 7x7 2-dimensional source field choices and the relationship to the 1-dimensional system.

NNLS solved the over determined system of equation (3) in least-squares subject to the constraint that $\phi_j \geq 0$. All fluence results were divided by the live-time of 5.0×10^4 seconds to arrive at results in units of flux (or differential flux in the case of the spectral technique). The resulting 2-dimensional image of the 511 keV gamma-ray line source (fitted-line technique) for the 5x5 source field choice is shown in Figures 6a and 6b for the fitted 511 keV single and multi-segment data, respectivel y. The point source is correctly seen in both figures at 1.5° from the center of rotation. With the single-segment data, the net source strength of the signal pixel is measured at (0.094±0.001) photons $cm^{-2}\,s^{-1}$ and is focused into a single pixel. With the multi-segment data, the net source strength is measured at (O. 101±0.006) photons $cm^{-2}\,s^{-1}$ with the signal distributed among three adjacent pixels, although still consistent with a point source. The integrated flux for the entire source field is (O. 1044.0.002)" photons $cm^{-2}\,s^{-1}$ and (O. 11 3±0.006) photons $cm^{-2}\,s^{-1}$ for the single and multi-segment data, respectively. These results compare to the expected value of 0.107 photons $cm^{-2}\,s^{-1}$ calculated for the calibrated ^{22}Na point source at a distance of 4.0 m.

The resulting 2-dimensional image for the 7x7 source field choice is shown in Figures 7a and 7b for the 511 keV single and multi-segment data, respectively. Again the point source is correctly seen in both Figures at 1.5° from the center of rotation. With the sing]c-segment data, the net source strength of the signal pixel is measured at (0.093+().()01) photons $cm^{-2}\,s^{-1}$ and is focused principally into a single pixel. However, a small amount of signal is seen in two adjacent pixels which if included brings the signal to (0.099±0.003) photons $cm^{-2}\,s^{-1}$. With the multi-segment data, the net source strength is measured at (O. 107± ().0()9) photons $cm^{-2}\,s^{-1}$ with the signal distributed among three adjacent pixels, again consistent with a point source. The integrated flux

for the entire source field is (O. 1 03±0.003) photons $cm^{-2}s^{-1}$ and ((). 1 1 0±0.009) photons $cm^{-2}s^{-1}$ for the single and mulli-segment data, respectively. These results arc consistent with the 5x5 results but achieve twice the image resolution. Both sets of results indicate that around 90% of the point source energy is deconvolved into a single pixel or adjacent pixels, with the remainder distributed within the instrument FOV.

The significant advantage of employing externally segmented germanium detectors is the ability to simultaneously perform imaging and high-resolution spectroscopy. This is illustrated in Figures 8a and 8b for the single- and multi-segment cases, respectively were the deconvolution is performed for each 1keV energy channel in the range from 400 keV to 600 keV (spectral technique). These figures show the spectra for the source-positioned pixel (center) and the eight surrounding pixels from the 7x7 field. The expected 511 keV line signal is seen predominantly in a single pixel for the single-segment data (Figure 8a) and in three adjacent pixels in the multi-segment data (Figure 8b). The FWHM of the observed 511 keV gamma-ray line is approximatel y 4 keV as expected for ^{22}Na annihilation radiation.

SUMMARY

Gamma-ray imaging measurements simultaneously with high-resolution spectroscopy have been performed using a coded aperture and an externally segmented germanium detector. Images of the 511 keV radiation emanating from a ^{22}Na sour-cc have been collected and fully two-dimensional imaging has been demonstrated with the source energy being focused onto a single pixel. “I-he sensitivity and energy resolution associated with germanium detectors is maintained in the imaging process, even when the image field is pushed beyond the intrinsic instrument resolution. Effects duc to Compton scattering in the detector and finite sour-cc distance can bc properly treated in the deconvolution process. on-going research includes extending this technique with a 12-segment detector.

ACKNOWLEDGMENTS

The research presented here was performed by the Jet Propulsion Laboratory, California Institute of Technology, under contract with the National Aeronautics and Space Administration.

REFERENCES

[1] L. S. Varnell, in Gamma-Ray Line Astrophysics, ed. Ph. Durouchoux and N. Prantzos, New York, AIP, 407, 1991.

[2] L. S. Varnell, J. C. Ling, W. A. Mahoney, A. S. Jacobson, R. H. Pehl, F. S. Goulding, D. A. Landis, P. N. Luke, and N. W. Madden, "A Position-Sensitive Germanium Detector for Gamma-Ray Astronomy", IEEE Trans. Nucl. Sci. 31,300-306, Feb. 1984.

[3] W. R. Cook, D. M. Palmer, T. A. Prince, S. M. Schindler, C. H. Starr, and E. C. Stone, "An imaging Observation of SN 1987A at Gamma-Ray Energies" Ap. J. 334,1.87-1.90, Nov. 1988.

[4] W. R. Cook, J. M. Grunsfeld, W. A. Heindl, D. M. Palmer, T. A. Prince, S. M. Schindler, C. H. Starr, and E. C. Stone, "Recent Results of Gamma-Ray Imaging Observations of the Galactic Center and Crab/A0535+26 Regions", Adv. Space Res. 11, 191-202, 1991.

[5] R. H. Dicke, "Scatter-Hole Cameras for X-Rays and Gamma Rays", Ap. J., 153, L101-L106, Aug. 1968.

[6] W. A. Wheaton, J. L. Callas, J. C. Ling, W. A. Mahoney, R. G. Radocinski, and L. S. Varnell, "The Rotating Coded Aperture: High-Resolution imaging spectroscopy for Gamma-Ray Astronomy", BAAS 22, 1261, 1990.

[7] P. N. Luke, "Gold-Mask Technique for Fabricating Segmented-Electrode Germanium Detectors", IEEE Trans. Nucl. Sci. 31,312-315, Feb. 1984.

[8] L. S. Varnell, J. C. Ling, W. A. Mahoney, R. H. Pehl, C. P. Cork, D. A. Landis, P. N. Luke, N. W. Madden, and D. F. Malone, in Nuclear Spectroscopy of Astrophysical Sources, eds N. Gehrels and G.H. Share, New York, AIP, 490, 1988.

[9] E. E. Fenimore and T. M. Cannon, "Coded Aperture Imaging with Uniformly Redundant Arrays", Applied Optics 17,337-347, Feb. 1978.

[10] J. L. Callas, W. A. Mahoney, L. S. Varnell and Wm. A. Wheaton, "High-Resolution Imaging Gamma-Ray Spectroscopy with Externally Segmented Germanium Detectors", Rev Sci. Instrum. 64, 143-153, Jan. 1993.

[11] L. D. Baumert, Cyclic Different Sets, Berlin, Springer-Verlag, 1971.

[12] J. A. Halbleib, R P, Kensek, T. A. Mehlhorn, G.D. Valdez, S, M. Seltzer and M. J. Berger, "1'1'S Version 3.0: The Integrated TIGER Series of Coupled Electron/Photon Monte Carlo Transport Codes", Sandia Report, SAND91- 1634, Mar. 1992.

13 G. W. Phillips, "HYPERMET", RSIC Peripheral Shielding Routine Collection, Oak Ridge Nat]. Lab., PSR-1OI , 1977.

14 Wm A. Wheaton, David D. Dixon, O. Tümay Tümer, and Allen D. Zych, "1.cast-Squares Deconvolution of Compton Telescope Data With the Positivity Constraint", internal JPL communication.

15 C. L. Lawson and R. J. Hanson, Solving Least-Squares Problems, New York, Prentice-Hall, 1974.

16 Suggested by D. Dixon of the University of California at Riverside.

FIGURE CAPTIONS

Figure 1. Diagram of the laboratory set up showing the relative position of the segmented detector (with cryostat) and coded aperture to the gamma-ray source. The spacing between the detector axis and the upstream face of the coded aperture is 40 cm. The coded aperture element widths are sized at 1.06 cm to match the average width of the detector segmentation. The detector segments and coded aperture elements are co-aligned. The intrinsic angular resolution is 1.06 cm/40 cm or 1.5°. The source is positioned 4.0 m upstream of the detector axis. The sour-cc field is rotated (equivalent to rotating the imaging system) to achieve the rotation modulation in the imaging systcm.

Figure 2. Deconvolved 1-dimensional image of Monte Carlo simulated 511 keV gamma-rays exhibiting the effects of a finite source-detector distance (4.0 m) as would be the case with a laboratory test. The effect can be corrected in the deconvolution process as illustrated by the figure results.

Figure 3. Measurement of the net Effective Area for each segment of the 5-segment detector at 511 keV for both the single-segment and multi-segment data sets. Segment 1 corresponds to the closed end of the detector; it is known to be larger than the other segments as reflected in the results. Note the expected lower efficiency of the end segments for the mu]ti-segment data[10].

Figure 4. Net full-energy-peak signal in the 5-segment detector from 511 keV gamma-rays viewed through the coded aperture at 0° of rotation for both the single-scgrncnt and multi-segment data sets. The relative position of the coded aperture at this rotational position is indicated. The expected modulation of the signal is apparent. Deviation in segment response from the ideal is mainly due to variations in segment thickness and performance. The anticipated filling-in of occulted segments is apparent in the rnulti-segment data. The live-time of this accumulation is 5.0×10^4 seconds.

Figure 5. Concept of the imaging system collecting a series of 1 -dimensional samples from a 2-dimensional sour-cc field as the system rotates through 180° for two choices of source field, a) 5x5 field of 1.5°×1.5° square pixels which matches the intrinsic resolution of the l-dimensional system and b) 7x7 field of ().75%0.75° square pixels which is finer than the intrinsic resolution of the 1-dimensional system.

Figure 6. Two-dimensional image (using the filtcd-line technique) of the 511 keV gamma rays from a point source imaged in the laboratory at JPL for the 5x5 source field choice with 1.5 °×1.5° pixel size using a) Single- and b) Multi-segment data. The source is correctly seen 1.5° from the center of rotation. The image has been corrected for finite distance effects in the deconvolution process.

Figure 7. Two-dimensional image (using the fitted-line technique) of the 511 keV gamma rays from a point source imaged in the laboratory at J] 'I. for the 7x7 source field choice with 0.75 °×0.75° pixel size using a) single and b) multi-segment data. The source is correctly seen 1.5° from the center of rotation. The image has been corrected for finite distance effects in the deconvolution process.

Figure 8. Spectra from 400 keV to 600 keV for the source-positioned pixel (center) and the eight surrounding pixels from the 7x7 field (deconvolved using the spectral technique) illustrating the excellent energy resolution simultaneously with gamma-ray imaging using a) single- and b) multi-segment data. The expected 511 keV line signal is seen predominantly in a single pixel for the single-scgrncnt data (a) and in three adjacent pixels in the multi-segment data (b).

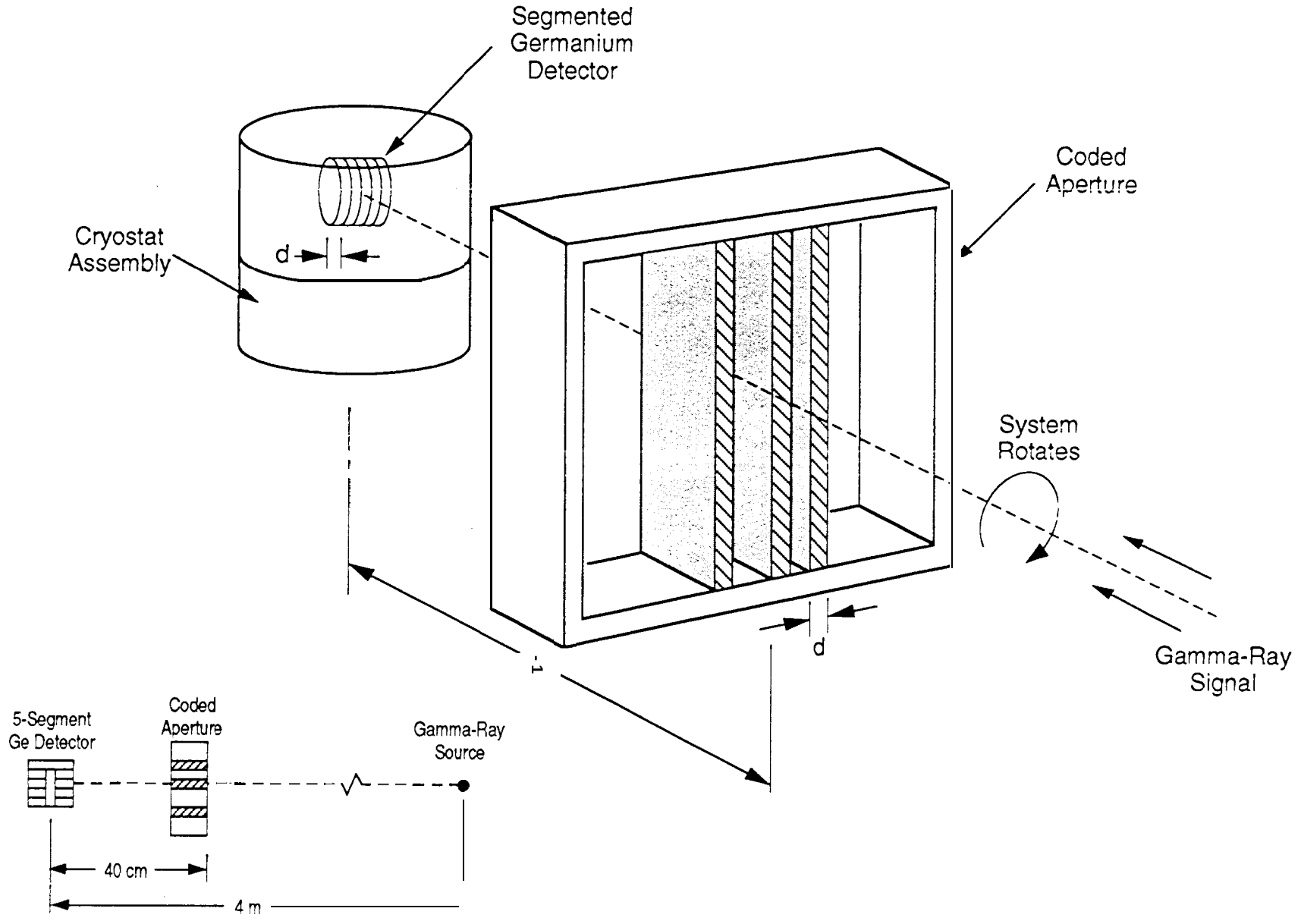
Segmented
Germanium
Detector
Coded
Aperture
Cryostat
Assembly
d
System
Rotates
d
-1
Gamma-Ray
Signal
5-Segment
Ge Detector
Coded
Aperture
Gamma-Ray
Source
40 cm
4 m

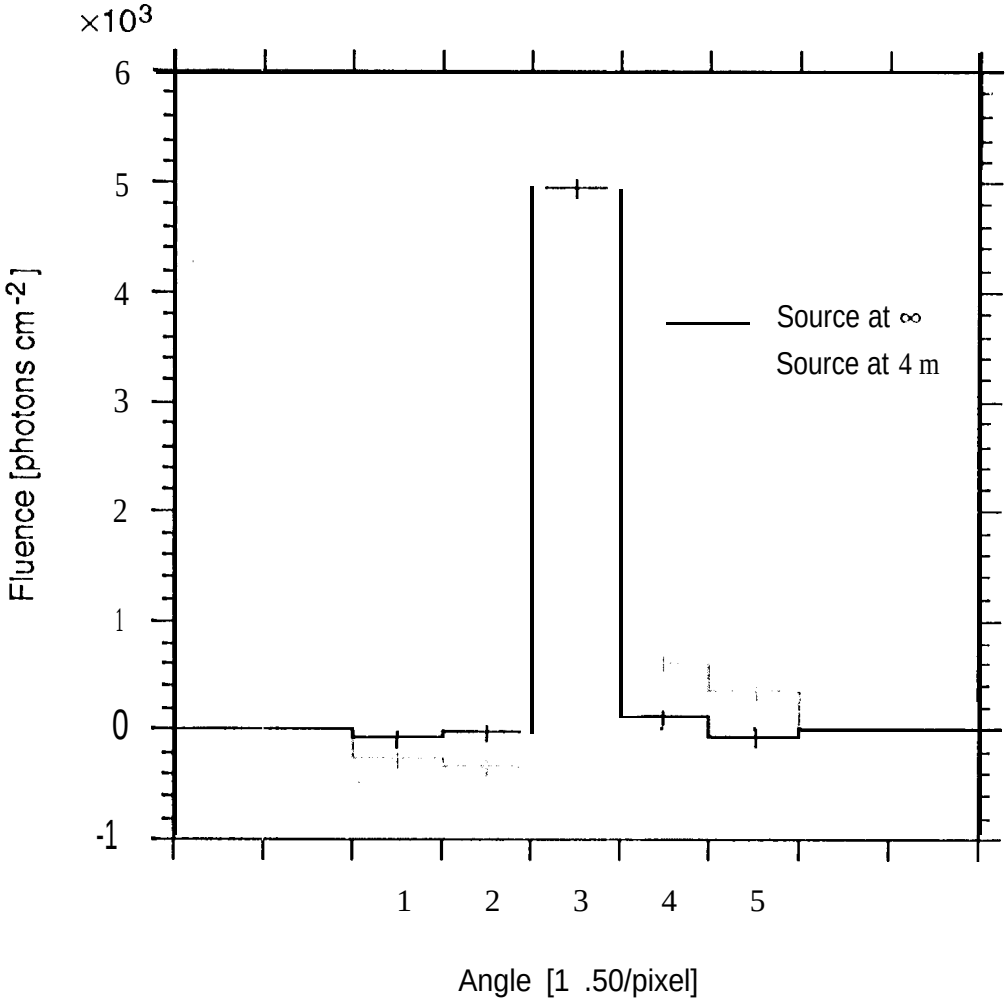
×10³
6
5
4
3
2
1
0
-1
Fluence [photons cm⁻²]
Source at ∞
Source at 4 m
1
2
3
4
5
Angle [1 .50/pixel]

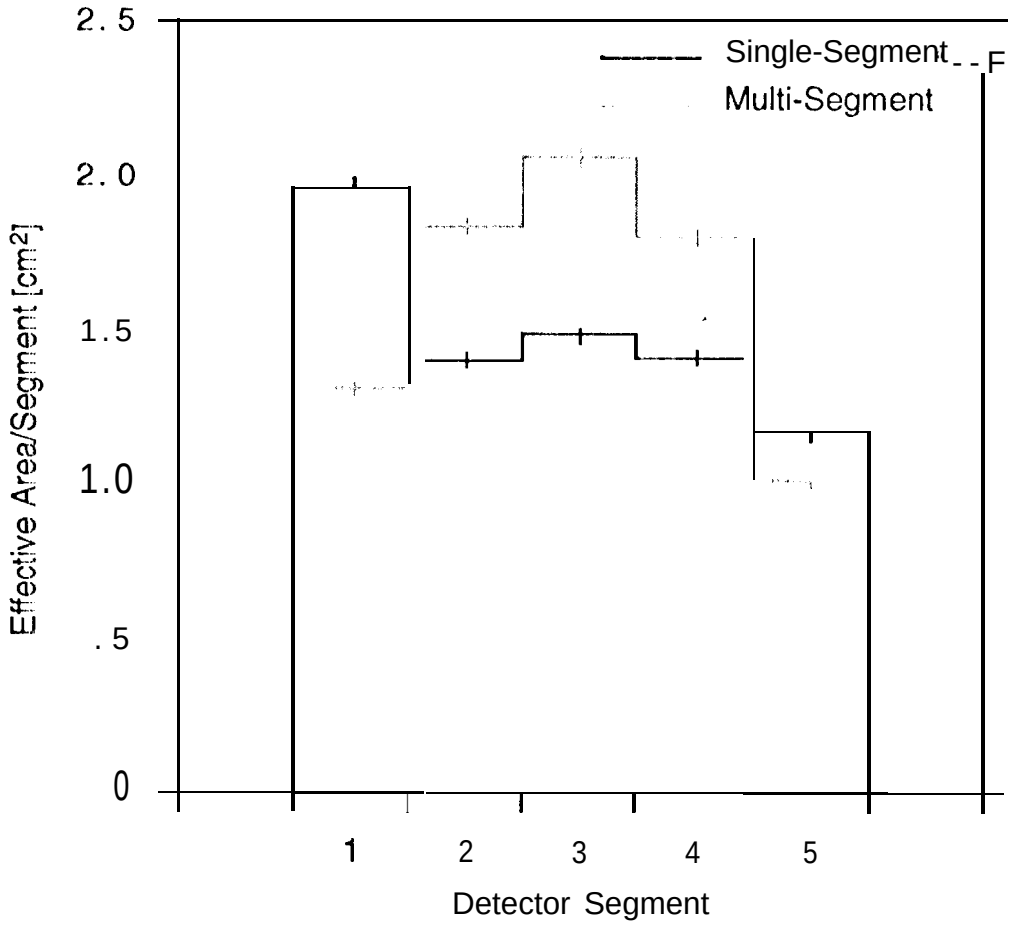
2.5
2.0
1.5
1.0
.5
0
Effective Area/Segment [cm2]
Single-Segment
Multi-Segment
1
2
3
4
5
Detector Segment

FIGURE 3

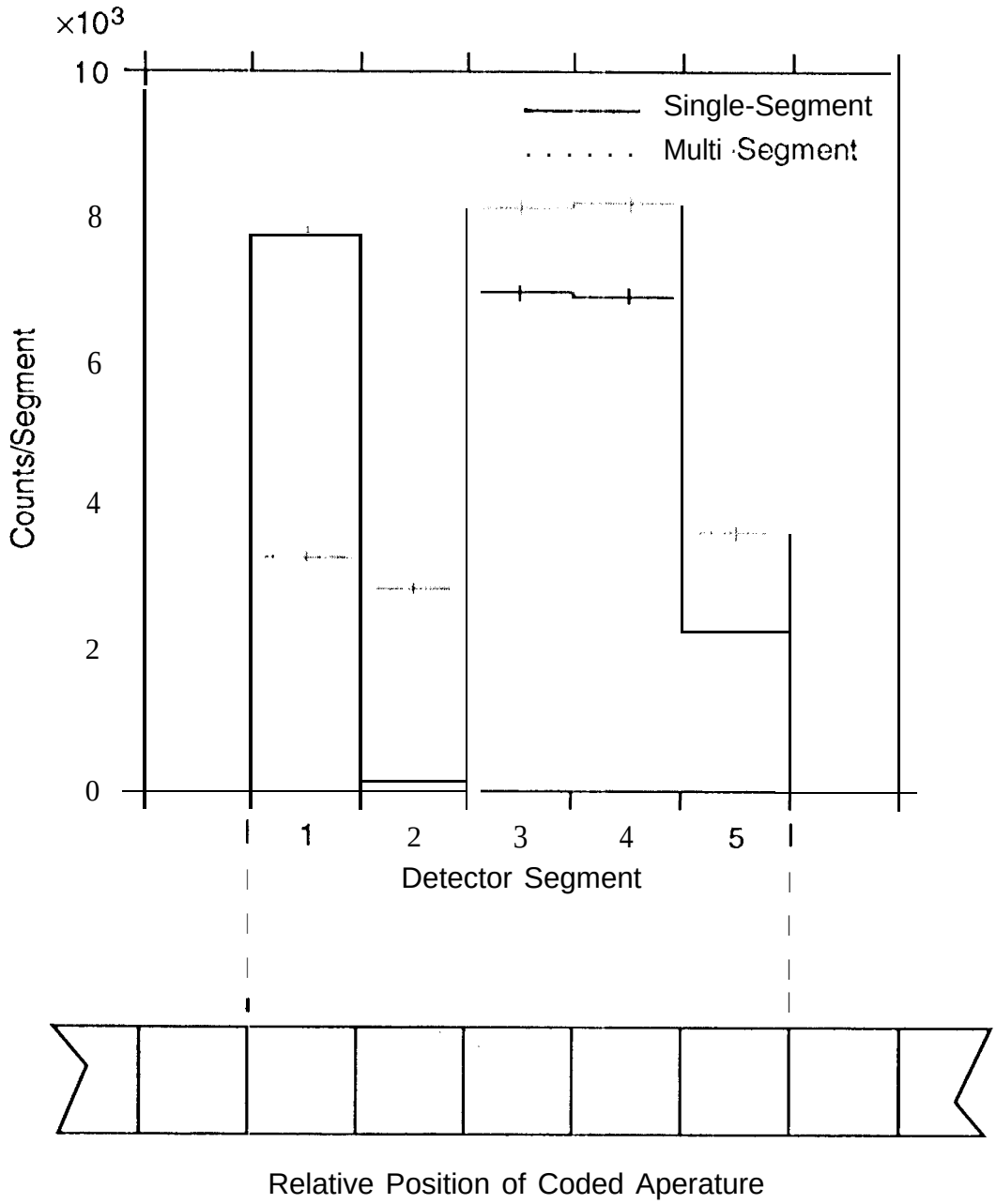
×10^3
10
8
6
4
2
0
Counts/Segment
Single-Segment
Multi-Segment
1
2
3
4
5
Detector Segment
Relative Position of Coded Aperature

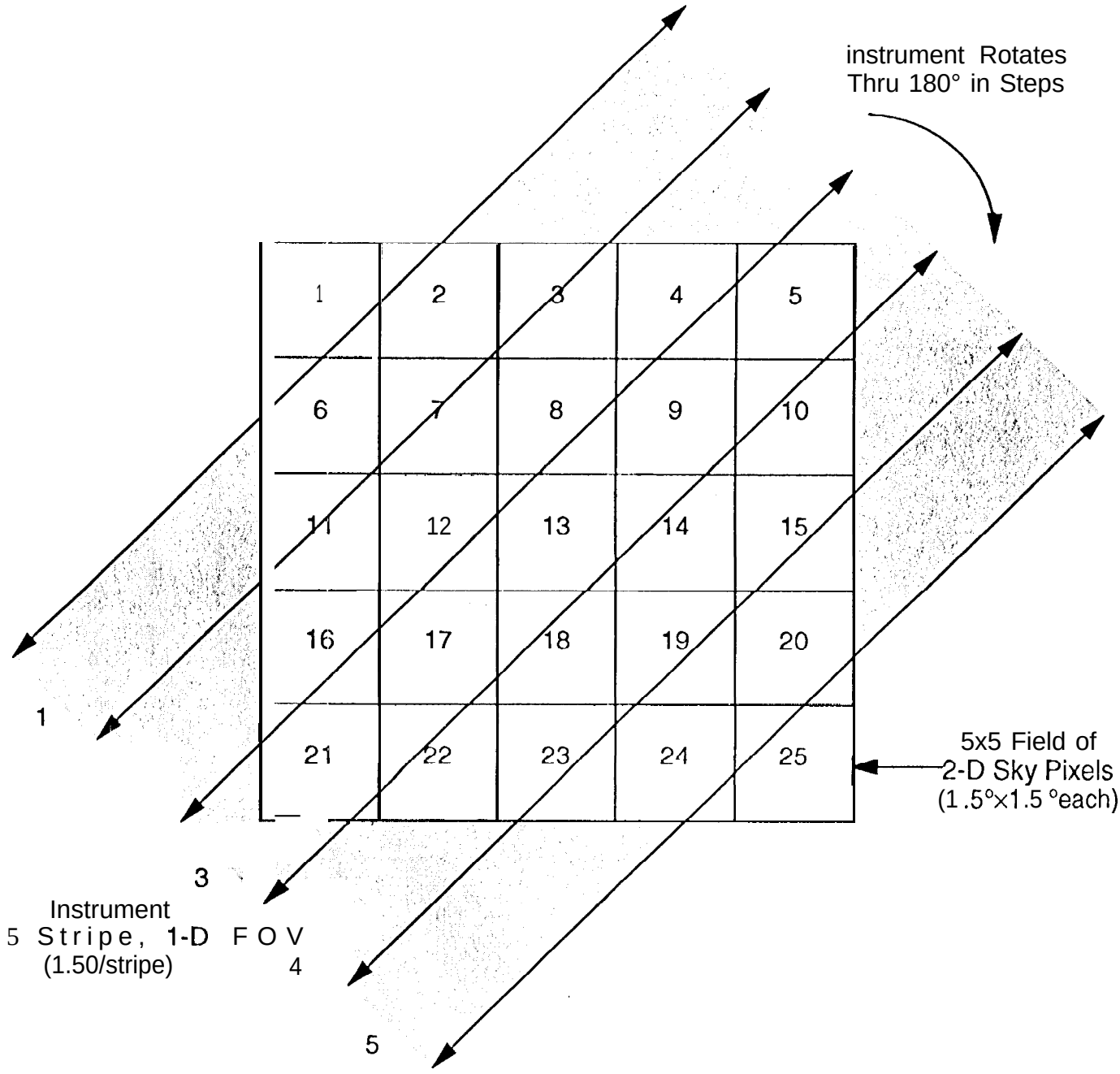
instrument Rotates
Thru 180° in Steps
1
2
3
4
5
6
7
8
9
10
11
12
13
14
15
16
17
18
19
20
21
22
23
24
25
5x5 Field of
2-D Sky Pixels
(1.5°×1.5 °each)
1
3
Instrument
5 Stripe, 1-D FOV
(1.50/stripe)
4
5

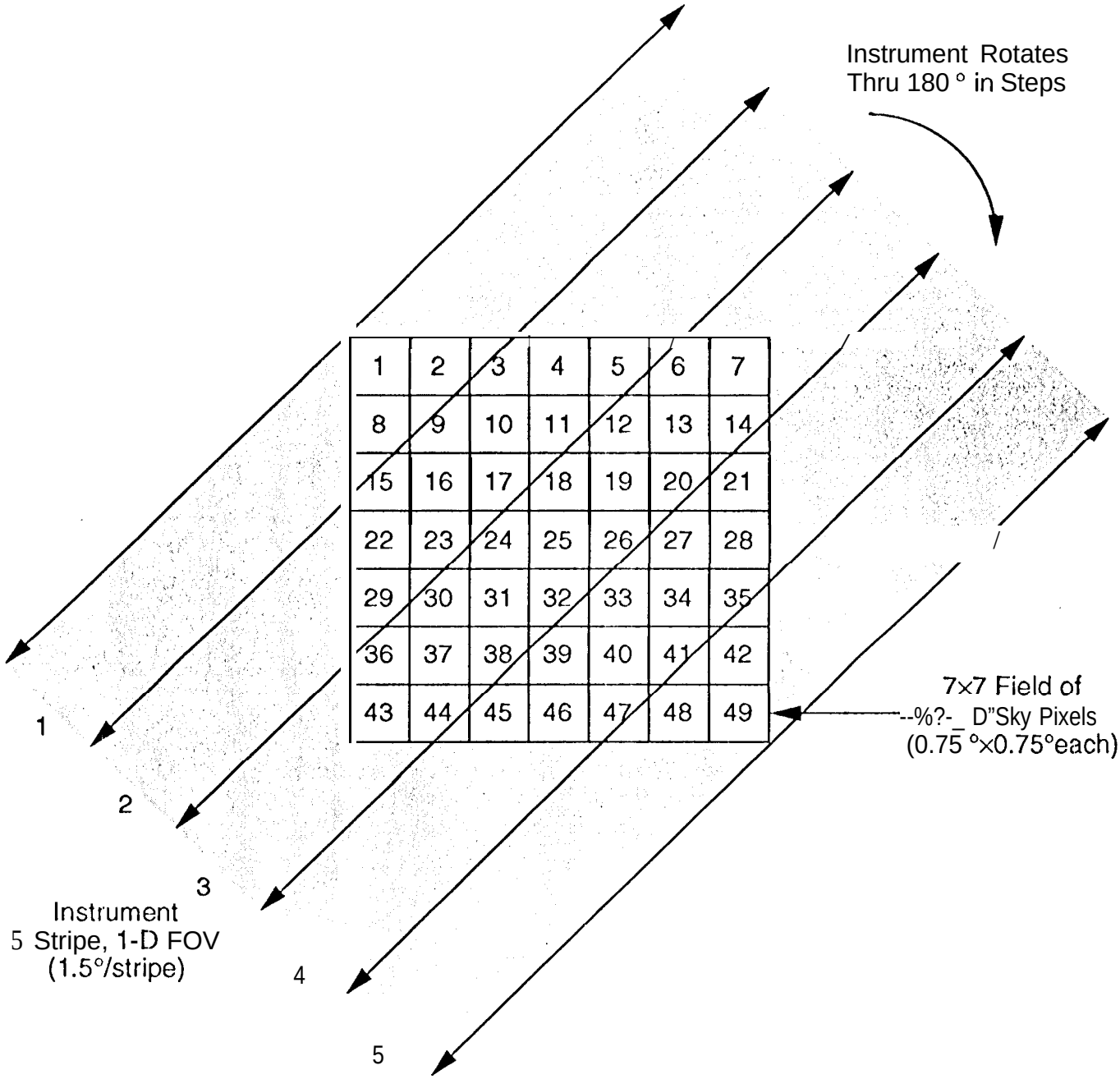
Instrument Rotates
Thru 180 ° in Steps
1 2 3 4 5 6 7
8 9 10 11 12 13 14
15 16 17 18 19 20 21
22 23 24 25 26 27 28
29 30 31 32 33 34 35
36 37 38 39 40 41 42
43 44 45 46 47 48 49
7×7 Field of
D"Sky Pixels
(0.75 °×0.75°each)
1
2
3
4
5
Instrument
5 Stripe, 1-D FOV
(1.5°/stripe)

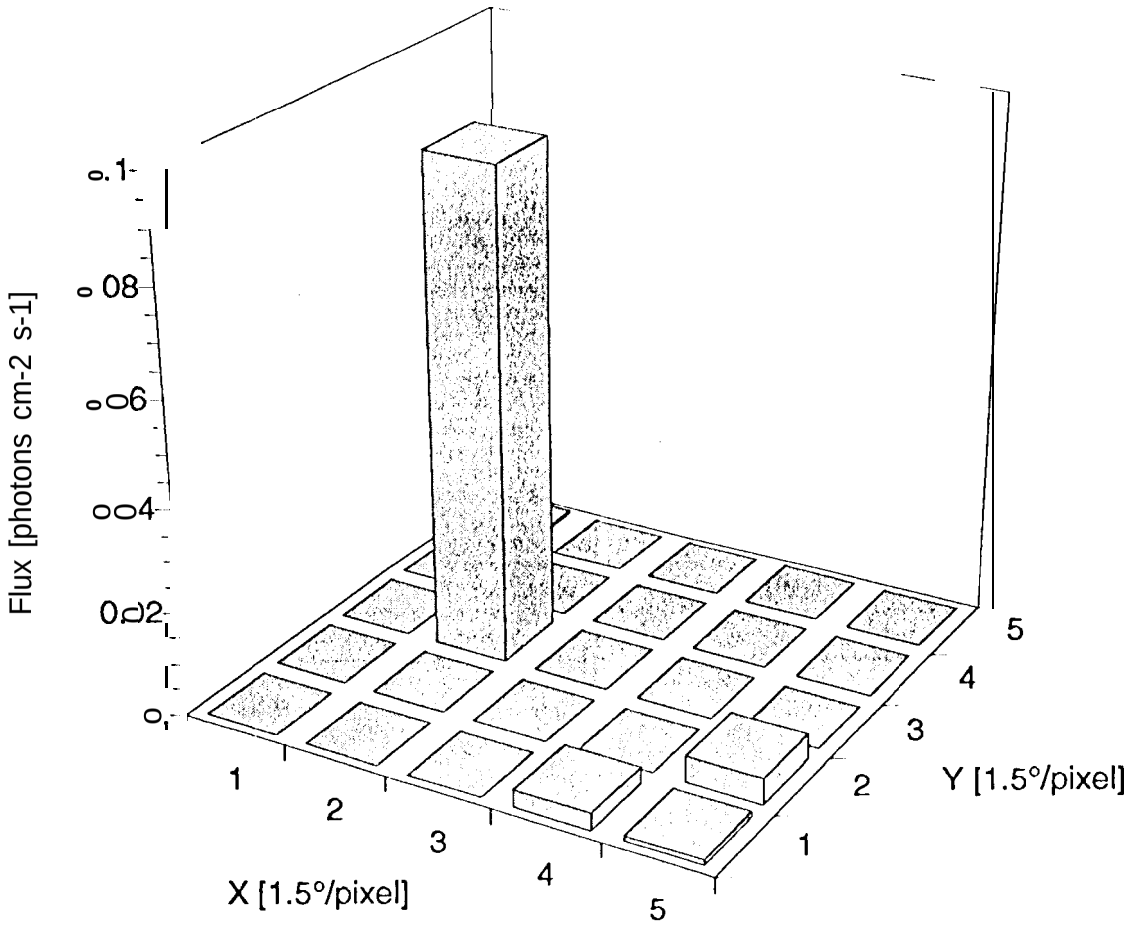
Flux [photons cm-2 s-1]
0.1
0.08
0.06
0.04
0.02
0
X [1.5°/pixel]
1
2
3
4
5
Y [1.5°/pixel]
1
2
3
4
5

Fig. 6a

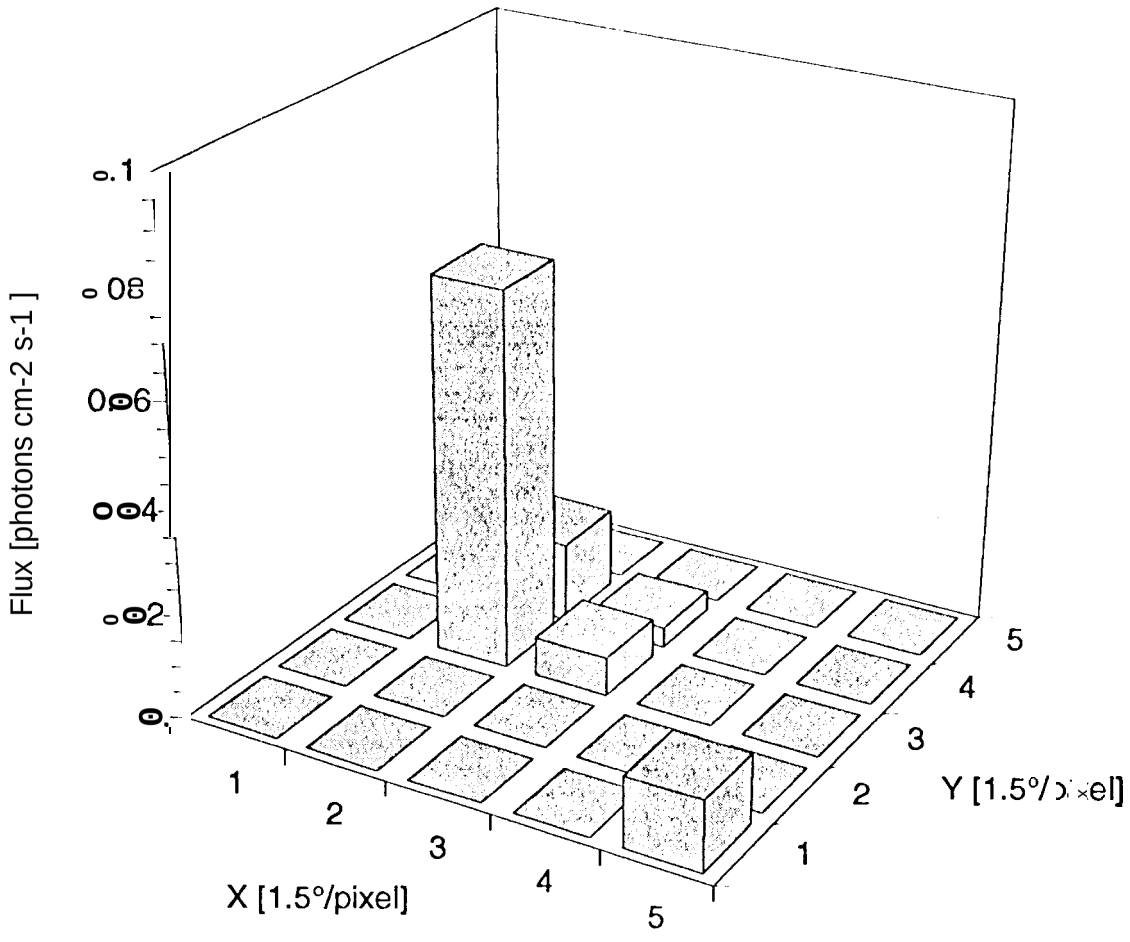
Flux [photons cm-2 s-1]
0.1
0.08
0.06
0.04
0.02
0
X [1.5°/pixel]
1
2
3
4
5
Y [1.5°/pixel]
1
2
3
4
5

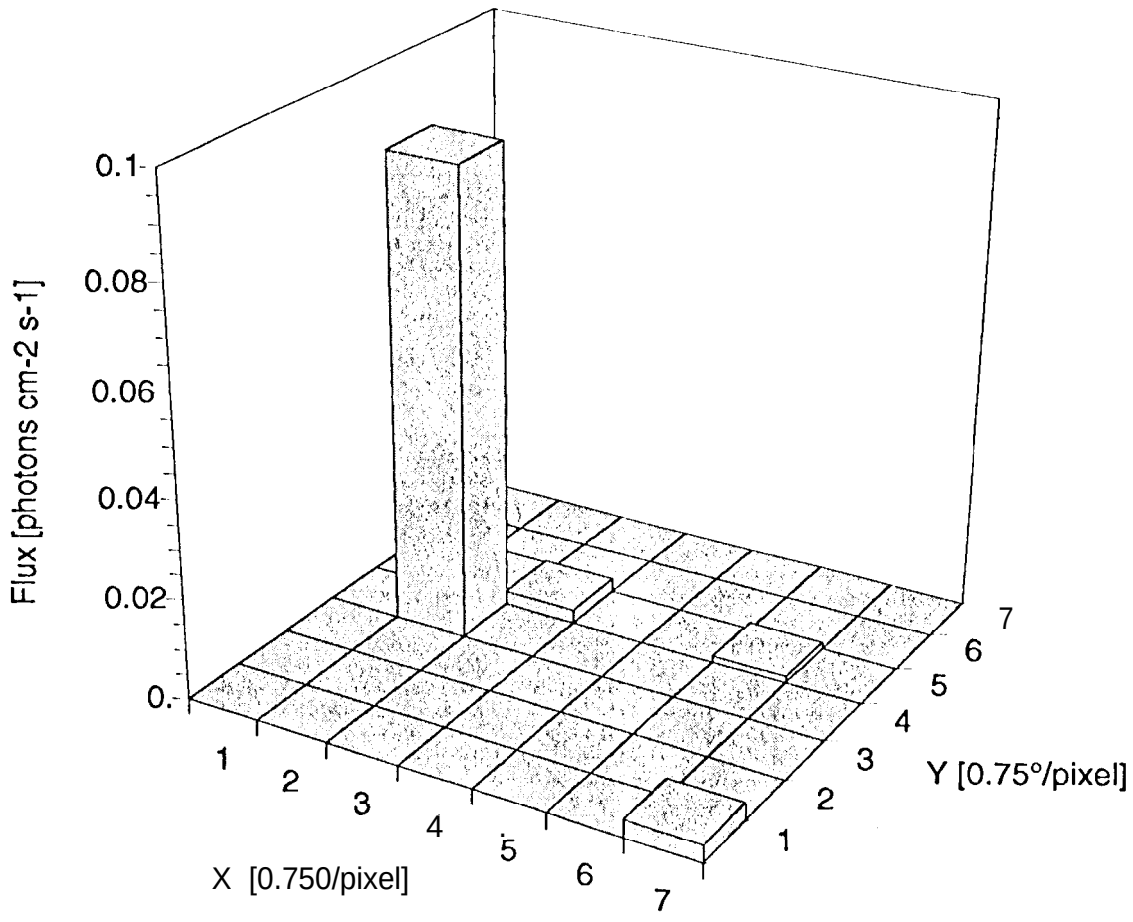
Flux [photons cm-2 s-1]
0.1
0.08
0.06
0.04
0.02
0.
1
2
3
4
5
6
7
X [0.750/pixel]
Y [0.75°/pixel]

Figure 7a

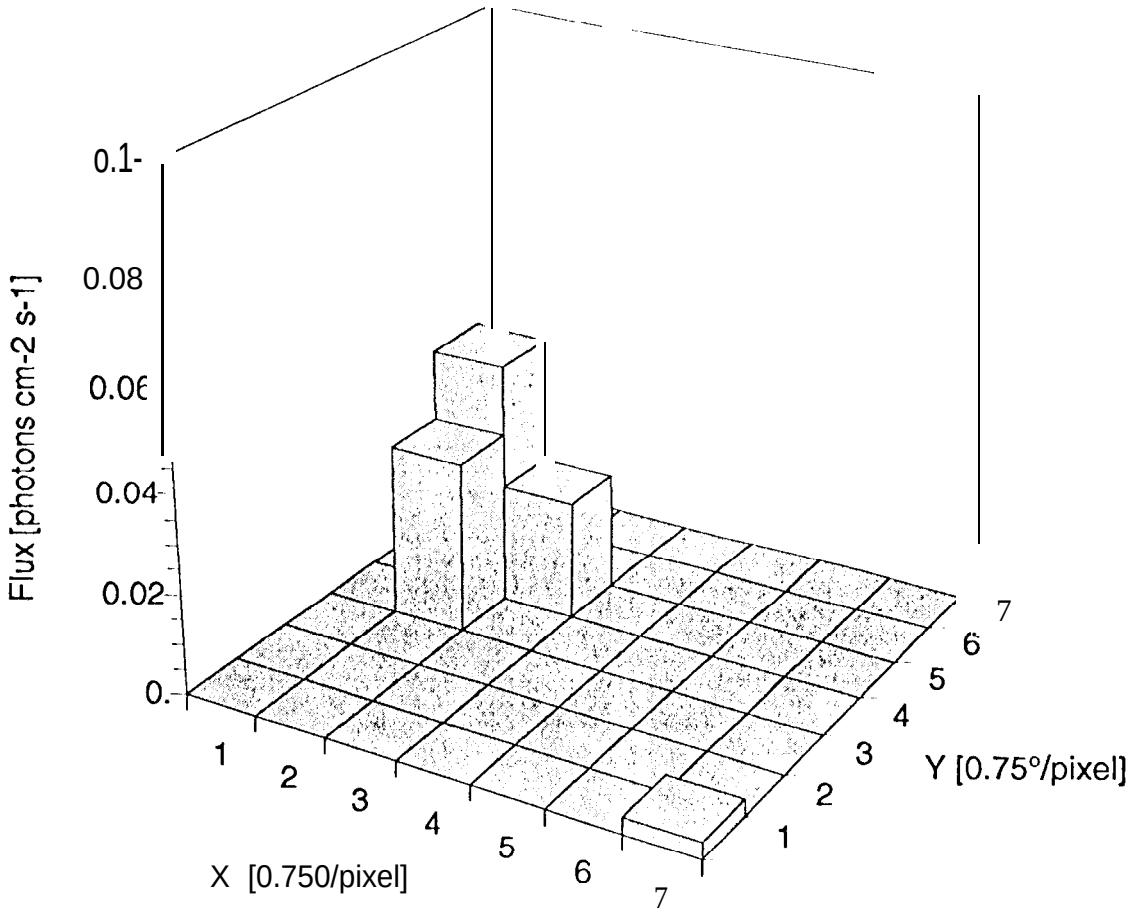
0.1
0.08
0.06
0.04
0.02
0.
Flux [photons cm-2 s-1]
1
2
3
4
5
6
7
X [0.750/pixel]
1
2
3
4
5
6
7
Y [0.75°/pixel]

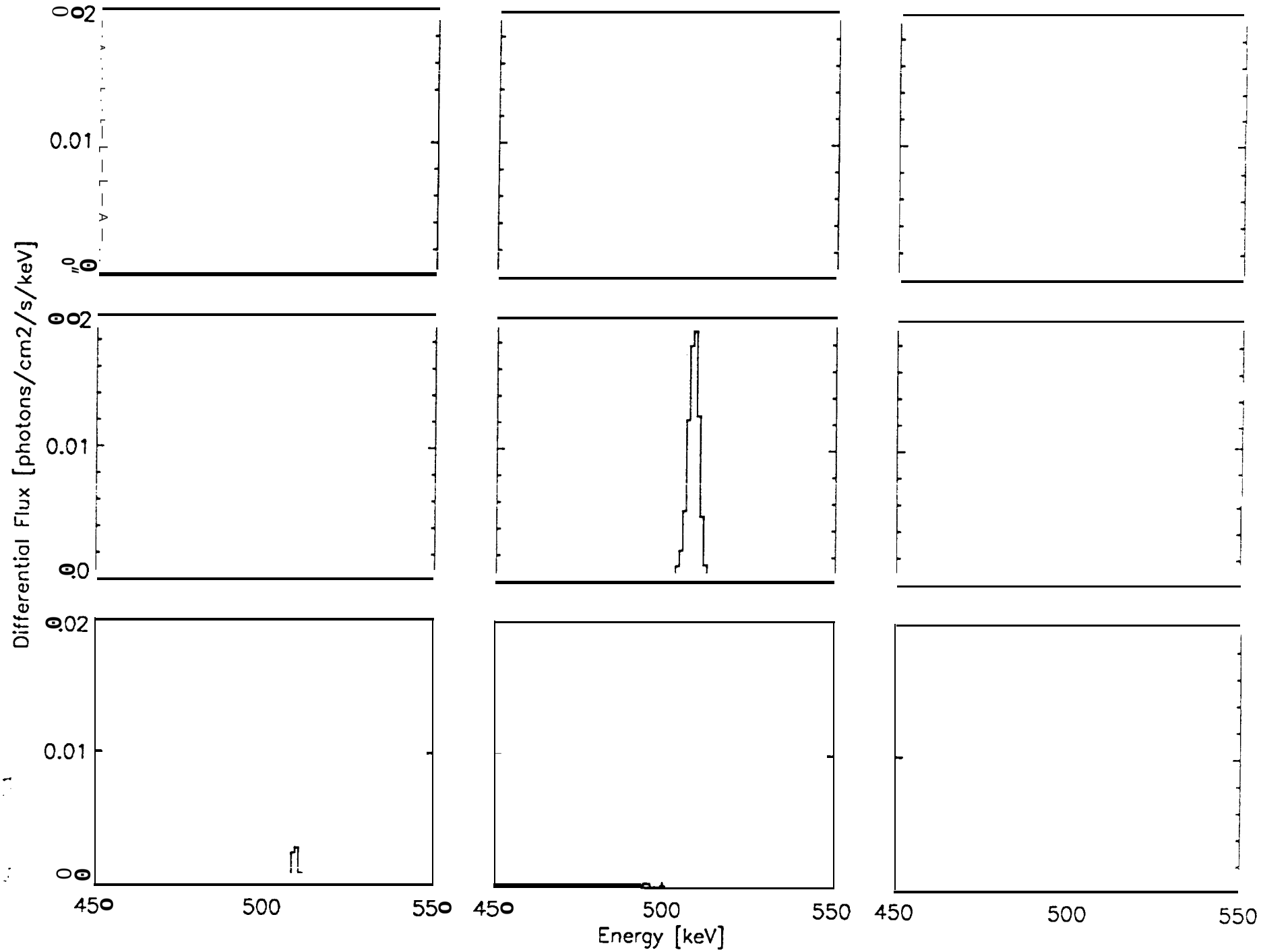
0.02
0.01
0
0.02
0.01
0
0.02
0.01
0
Differential Flux [photons/cm2/s/keV]
450
500
550
450
500
550
450
500
550
Energy [keV]

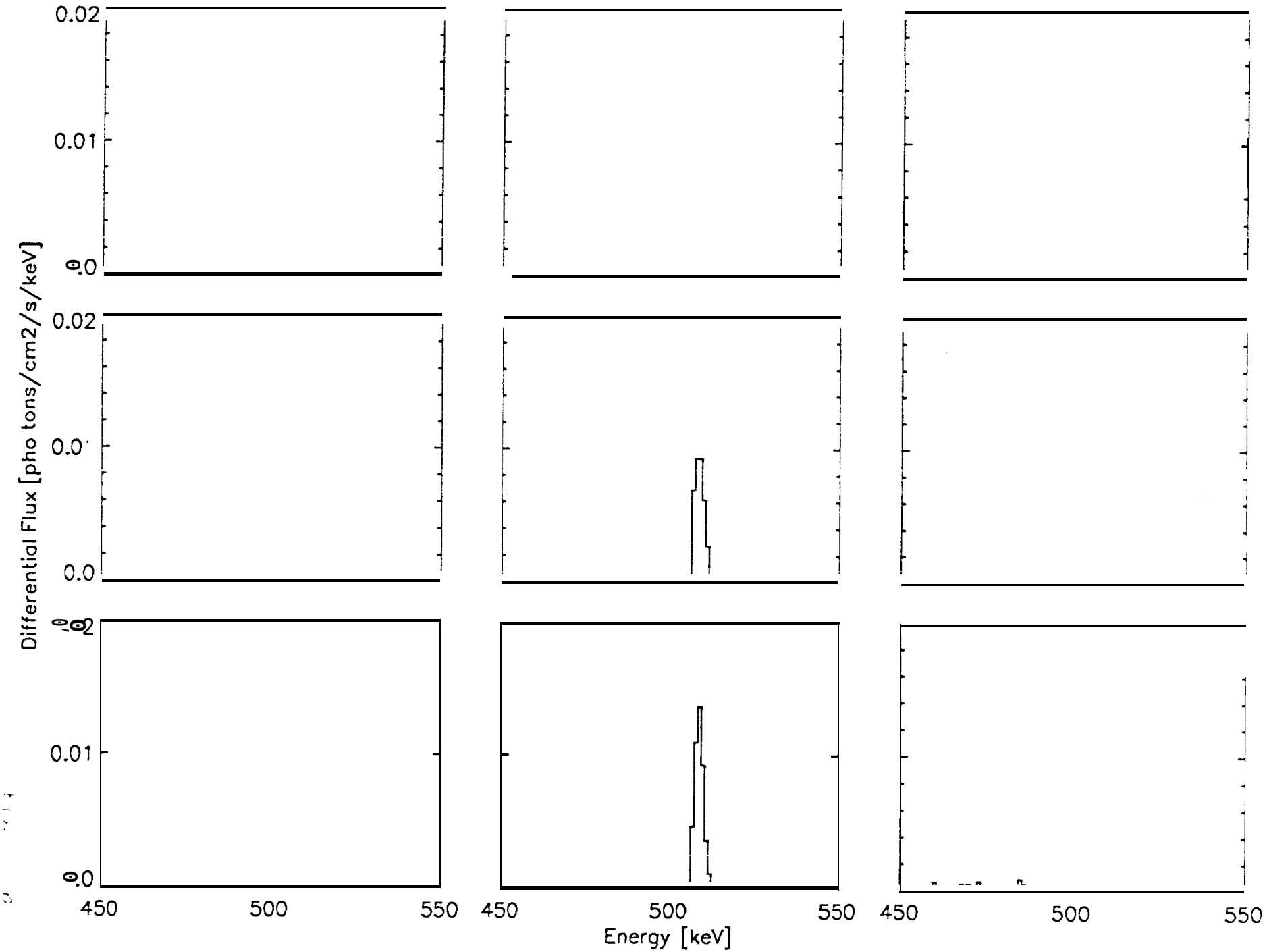
0.02
0.01
0.0
0.02
0.0
0.02
0.01
0.0
Differential Flux [pho tons/cm2/s/keV]
450
500
550
450
500
550
450
500
550
Energy [keV]